Inorganic Chemistry

Article

pubs.acs.org/IC

Insight into the Structure and Functional Application of the $Sr_{0.95}Ce_{0.05}CoO_{3-\delta}$ Cathode for Solid Oxide Fuel Cells

Wei Yang,[†] Huairuo Zhang,[‡] Chunwen Sun,*[,†] Lilu Liu,[†] J. A. Alonso,*[,§] M. T. Fernández-Díaz,[∥] and Liquan Chen[†]

[†]Key Laboratory for Renewable Energy, Beijing Key Laboratory for New Energy Materials and Devices, Beijing National Laboratory for Condensed Matter Physics, Institute of Physics, Chinese Academy of Sciences, Beijing 100190, China

[§]Instituto de Ciencia de Materiales de Madrid, CSIC, 28049 Cantoblanco, Madrid, Spain

[∥]Institut Laue Langevin, BP 156X, Grenoble Cedex, France

[‡]Department of Materials Science and Engineering, University of Sheffield, Sir Robert Hadfield Building, Mappin Street, Sheffield S1 3JD, U.K.

Supporting Information

ABSTRACT: A new perovskite cathode, $Sr_{0.95}Ce_{0.05}CoO_{3-\delta}$, performs well for oxygen-reduction reactions in solid oxide fuel cells (SOFCs). We gain insight into the crystal structure of $Sr_{1-x}Ce_xCoO_{3-\delta}$ (x = 0.05, 0.1) and temperature-dependent structural evolution of $Sr_{0.95}Ce_{0.05}CoO_{3-\delta}$ by X-ray diffraction, neutron powder diffraction, and scanning transmission electron microscopy experiments. $Sr_{0.9}Ce_{0.1}CoO_{3-\delta}$ shows a perfectly cubic structure ($a = a_0$), with a large oxygen deficiency in a single oxygen site; however, $Sr_{0.95}Ce_{0.05}CoO_{3-\delta}$ exhibits a tetragonal perovskite superstructure with a double c axis, defined in the $P4/mmm$ space group, that contains two crystallographically different cobalt positions, with distinct oxygen environments. The structural evolution of $Sr_{0.95}Ce_{0.05}CoO_{3-\delta}$ at high temperatures was further studied by in situ temperature-dependent NPD experiments. At 1100 K, the oxygen atoms in $Sr_{0.95}Ce_{0.05}CoO_{3-\delta}$ show large and highly anisotropic displacement factors, suggesting a significant ionic mobility. The test cell with a $La_{0.8}Sr_{0.2}Ga_{0.83}Mg_{0.17}O_{3-\delta}$-electrolyte-supported (~300 μm thickness) configuration yields peak power densities of 0.25 and 0.48 W cm^{-2} at temperatures of 1023 and 1073 K, respectively, with pure H_2 as the fuel and ambient air as the oxidant. The electrochemical impedance spectra evolution with time of the symmetric cathode fuel cell measured at 1073 K shows that the $Sr_{0.95}Ce_{0.05}CoO_{3-\delta}$ cathode possesses superior ORR catalytic activity and long-term stability. Mixed ionic−electronic conduction properties of $Sr_{0.95}Ce_{0.05}CoO_{3-\delta}$ account for its good performance as an oxygen-reduction catalyst.

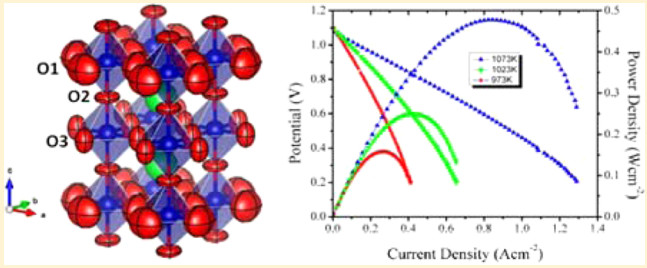

1. INTRODUCTION

The development of mixed ionic−electronic conductors (MIECs) as electrodes in solid oxide fuel cells (SOFCs) with adequate performance is one of the challenges to reduce the SOFC operating temperature without detriment to the cell performance.[1] $SrCoO_{3-\delta}$ presents two polymorphs, 3C-cubic and 2H-hexagonal; among them, the former (high-temperature phase) exhibits a high electrical conductivity and oxygen permeation flux.[2−4] Unfortunately, below 900 °C, a phase transition to the 2H-hexagonal polymorph (lacking the desired conduction properties) is promoted during slow cooling of the sample. A 3C-$SrCoO_{3-\delta}$ perovskite can be stabilized in a wider temperature range by subtle doping of the perovskite framework, thus avoiding the transition to the hexagonal phase and keeping adequate mixed ionic−electronic conduction properties, which are essential for an oxygen-reduction catalyst in intermediate-temperature SOFCs, unaltered. This aim may be achieved by replacing either strontium by barium, lanthanum, samarium, etc.,[5] or cobalt by scandium, iron, nickel, etc.[6,7] Stabilization of the cubic structure drives an increment of the oxygen diffusion, as demonstrated in tantalum-doped $SrCoO_{3-\delta}$, with excellent oxygen permeation flux predominated by oxygen ion bulk diffusion, which finds applications in oxygen separation membranes.[8] Following this strategy, we have stabilized in a previous work a 3C perovskite phase by doping the $SrCoO_{3-\delta}$ system with M^{n+} = Sb^{5+} or Mo^{6+} in $SrCo_{1-x}M_xO_{3-\delta}$ (x = 0.05, 0.1, 0.15, 0.2).[9,10]

Recently, we have prepared $Sr_{1-x}Ce_xCoO_{3-\delta}$ ($0.05 \le x \le 0.15$) perovskite oxides by a sol−gel method and studied them as cathodes for intermediate-temperature SOFCs.[11] In fact, the Sr−Ce−Co−O system had been previously investigated from some points of view: In a pioneering work, Trofimenko et al.[12] showed that the cerium solubility is very narrow because it is limited to 15%. Later on, James et al.[13] studied the structure and magnetism in the oxygen-deficient $Sr_{1-x}Ce_xCoO_{3-\delta}$

Received: January 7, 2015
Published: March 10, 2015

DOI: 10.1021/acs.inorgchem.5b00051
Inorg. Chem. 2015, 54, 3477−3484

perovskites; Maignan et al.[14] found that the most metallic composition of $Sr_{1-x}Ce_xCoO_{3-\delta}$ corresponds to $x = 0.05$ and $\delta \approx 0.28$. Wei et al. studied the high-temperature electrical properties of cerium-doped $SrCoO_{3-\delta}$. It was found that the conductivity of $Sr_{1-x}Ce_xCoO_{3-\delta}$ is enhanced as the cerium content increases within the solubility limit.[15] A conductivity of over 500 S cm^{-1} was obtained for $x = 0.15$ for testing at 623−673 K for a sample sintered at 1373 K. Additionally, the $Sr_{0.95}Ce_{0.05}CoO_{3-\delta}$ perovskite, combined with copper nanoparticles, has been recently studied as an excellent bifunctional catalyst for lithium−air batteries[16] or lithium−water batteries.[17]

As SOFC cathodes, $Sr_{1-x}Ce_xCoO_{3-\delta}$ materials have sufficiently high electronic conductivities and excellent chemical compatibility with the SDC electrolyte.[11] The peak power density of the cell with the $Sr_{0.95}Ce_{0.05}CoO_{3-\delta}$ cathode reaches 0.625 W cm^{-2} at 973 K in an anode-supported configuration, with an electrolyte layer thinner than 45 μm.[11]

In order to establish structure−property correlations, we performed a neutron powder diffraction (NPD) study of the crystal structure of these materials and their thermal evolution from room temperature (RT) to 1100 K. The results are quite interesting: whereas for $Sr_{0.9}Ce_{0.1}CoO_{3-\delta}$ we observe a perfect cubic structure ($a = a_0$), with a large oxygen deficiency in a single oxygen site, for $Sr_{0.95}Ce_{0.05}CoO_{3-\delta}$, there are tiny superstructure peaks indicating a tetragonal structure ($a_0 \times a_0 \times 2a_0$) due to the long distance ordering of the oxygen vacancies, with two kinds of cobalt atoms with different oxidation states. The implications of these findings in the performance of the mentioned materials are discussed.

2. EXPERIMENTAL SECTION

2.1. Synthesis of Materials. Synthesis of $Sr_{1-x}Ce_xCoO_{3-\delta}$ ($x = 0.05$, 0.10) was carried out by a typical sol−gel method from stoichiometric amounts of analytical-reagent-grade $Sr(NO_3)_2$, $Co(NO_3)_2{\cdot}6H_2O$, and $Ce(NO_3)_3{\cdot}6H_2O$ dissolved in citric acid with the further addition of ethylene glycol. The pink solution was stirred for 10 h at 353 K on a hot plate, becoming a stiff gel. The brown gel was dried in an electric oven at 523 K to obtain a dark-gray precursor. Then the precursor was pelletized and calcined first at 1273 K and then 1373 K for 5 h in air to get the samples.

2.2. Structural Characterizations. The reaction products were characterized by X-ray diffraction (XRD) for phase identification and assessment of the phase purity. Characterization was performed with a Bruker-AXS D8 diffractometer (40 kV, 30 mA) in Bragg−Brentano reflection geometry with Cu Kα radiation (λ = 1.5418 Å). The chemical compatibility between $Sr_{1-x}Ce_xCoO_{3-\delta}$ and lanthanum/strontium/gallium/magnesium oxide (LSGM) was studied by grinding both powders in equal weight amounts and calcining for 5 h at 1373 K in air and then checked by XRD.

A JEOL 2100F scanning transmission electron microscope (JEOL, Tokyo, Japan) equipped with a CEOS (Heidelberg, Germany) probe aberration corrector was used for atomic resolution analysis on the order/disorder of oxygen-ion vacancies.

NPD data were collected at RT in the D2B diffractometer at the Institut Laue Langevin (Grenoble, France). A high-intensity mode ($\Delta d/d \geq 2 \times 10^{-3}$) was selected, with a neutron wavelength λ = 1.594 Å within the angular 2θ range from 5° to 165°. For the temperature-dependent diffraction study, NPD patterns were collected with the HRPT high-resolution diffractometer at the SINQ spallation source at the Paul-Scherrer Institute (Villigen, Switzerland). A shorter wavelength was utilized (λ = 1.1545 Å) to be able to access a wider region of the reciprocal space and make anisotropic refinement for the oxygen positions of the investigated perovskite oxide possible. About 2 g of the sample was contained in a vanadium tube placed in the isothermal zone of a furnace with a vanadium resistor operating under vacuum ($P_{O_2} \approx 10^{-6}$ Torr). Measurements were carried out in air at 300, 700, 900, and 1100 K. After the high-temperature study, a new pattern was collected at 300 K, with λ = 1.494 Å. The collection time was 2 h per pattern. The diffraction data were all analyzed by the Rietveld method with the *FULLPROF* program[18] and the use of its internal tables for scattering lengths. The line shape of the diffraction peaks was generated by a pseudo-Voigt function. The irregular background coming from the quartz container was extrapolated from points devoid of reflections. In the final run, the following parameters were refined: background points, zero shift, half-width, pseudo-Voigt, and asymmetry parameters for the peak shape, scale factor and unit-cell parameters. Positional and occupancy factors for oxygen atoms and isotropic thermal factors (anisotropic for oxygen atoms for high-temperature data) were also refined for the NPD data. The coherent scattering lengths for strontium, cerium, cobalt, and oxygen were 7.02, 4.84, 2.49, and 5.803 fm, respectively.

2.3. Fabrication and Testing of Cells. LSGM-electrolyte-supported cells were fabricated to test the electrochemical performance and evaluate the stability of the cathode. $La_{0.9}Sr_{0.1}Ga_{0.8}Mg_{0.2}O_{3-\delta}$ (LSGM, 99.9%) powder was purchased from Praxair Inc. and used without further treatment. Dense LSGM pellets were obtained after sintering LSGM disks at 1723 K for 10 h. The obtained pellets were then polished with a diamond wheel to about 300 μm thickness.

For symmetric cells, the as-synthesized samples were first thoroughly mixed with $Sm_{0.2}Ce_{0.8}O_{1.9}$, ethyl cellulose, and α-terpinol to form composite cathode pastes. The cathode pastes were then screen-printed onto both sides of the dense LSGM electrolyte and then calcined at 1343 K for 2 h.

For single cells, the anode paste was first prepared by mixing NiO, SDC, and corn starch in a weight ratio of 65:35:20 with the addition of a 6 wt % ethyl cellulose and α-terpinol solution. In order to avoid reactions between nickel and the LSGM electrolyte, a thin layer of a $Ce_{0.8}La_{0.2}O_{2-\delta}$ (LDC) barrier layer was used as a buffer layer between the electrode and electrolyte to prevent cation migration. The LDC layer was calcined at 1573 K for 1 h. The anode paste was then screen-printed onto the LDC layer, followed by drying and calcining at 1523 K for 2 h. The cathodes were fabricated using the same procedures as those described for the symmetric cells.

Electrochemical impedance spectroscopy (EIS) measurements were carried out with a SOLARTRON electrochemical workstation (1260A FRA). A symmetric cell SCCO|LSGM|SCCO was used for EIS measurements. The stability of the cathodes in symmetric cells was monitored at 1073 K with different time intervals. For single cells, the green anodes were first reduced in situ from NiO-SDC to Ni-SDC cermet anodes, and then the cells were tested with humidified (3 wt % H_2O) H_2 as the fuel in the anode side and ambient air as the oxidant in the cathode side, using a SOLARTRON electrochemical workstation (1287A interface) in the temperature range of 973−1073 K.

3. RESULTS AND DISCUSSION

3.1. Crystallographic Characterization of $Sr_{1-x}Ce_xCoO_{3-\delta}$ (x = 0.05, 0.1) at RT. Figure 1 shows the XRD patterns of the as-synthesized $Sr_{1-x}Ce_xCoO_{3-\delta}$ (x = 0.05, 0.1) at RT, which show pure, well-crystallized perovskite phases, indexed in a cubic unit cell with a = ∼3.87 Å for both materials.

A NPD study at RT (300 K) was essential to unveiling the true symmetry of these oxides. Whereas for $x = 0.1$ the NPD pattern confirms the cubic symmetry, with a large oxygen deficiency in a single oxygen site (refined composition $Sr_{0.90}Ce_{0.10}CoO_{2.75(1)}$), for $x = 0.05$, the NPD diagram conspicuously shows a tetragonal superstructure with doubled c axis, as $a = b \approx a_0$ and $c \approx 2a_0$. This superstructure is manifested by extremely weak reflections, as shown in Figure S1 in the Supporting Information (SI). A similar superstructure was formerly described for $SrCo_{0.9}Sb_{0.1}O_{3-\delta}$,[9] $SrCo_{0.9}Mo_{0.1}O_{3-\delta}$,[10] and $SrCo_{0.95}Sb_{0.05}O_{3-\delta}$.[19] Following this model, the structure was defined in the $P4/mmm$ space group

DOI: 10.1021/acs.inorgchem.5b00051
Inorg. Chem. 2015, 54, 3477−3484

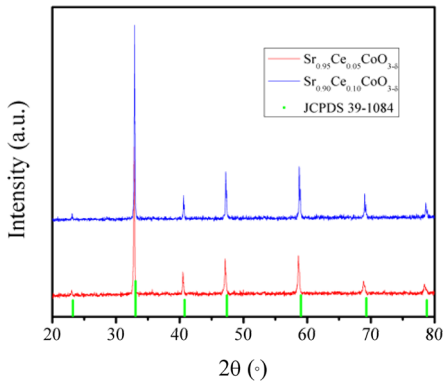

Figure 1. Powder XRD patterns of the as-synthesized $Sr_{0.90}Ce_{0.10}CoO_{3-\delta}$ and $Sr_{0.95}Ce_{0.05}CoO_{3-\delta}$ at RT.

with strontium and cerium distributed at random at 2h ($^1/_2$, $^1/_2$, z) sites, cobalt at 1a (0, 0, 0) (labeled Co1) and 1b (0, 0, $^1/_2$) (labeled Co2) sites, and three inequivalent types of oxygen atoms, O1 at 2f ($^1/_2$, 0, 0), O2 at 2g (0, 0, z), and O3 at 2e ($^1/_2$, 0, $^1/_2$). The presence of oxygen vacancies at the three types of oxygen positions was tested. For O1, the occupancy factors converged to unity [e.g., 1.02(2)]; however, O2 and O3 indeed exhibited significant oxygen deficiency [i.e., 0.946(4) for O2 and 0.825(2) for O3]. The crystallographic formula derived from the RT NPD data is $Sr_{0.95}Ce_{0.05}CoO_{2.768(3)}$. The good agreement between the observed and calculated profiles is displayed in Figure 2a for the x = 0.1 and 0.05 patterns at RT, and Figure 2b illustrates the cubic and tetragonal crystal structures; the final structural parameters and agreement factors are gathered at Table S1 in the SI for these two perovskite oxides at RT.

3.2. Temperature-Dependent Structural Evolution for $Sr_{0.95}Ce_{0.05}CoO_{3-\delta}$. In our previous study, the cell with the $Sr_{0.95}Ce_{0.05}CoO_{3-\delta}$ cathode showed a substantially higher power density than that with the $Sr_{0.90}Ce_{0.10}CoO_{3-\delta}$ cathode.[11] It seems that the tetragonal symmetry is more efficient to catalyze the oxygen-reduction process happening at the cathodic side of the cell; a temperature-dependent NPD study appeared to be crucial to understanding the crystal structure evolution of $Sr_{0.95}Ce_{0.05}CoO_{3-\delta}$ at the working temperatures of the intermediate-temperature SOFC, especially when a transition from tetragonal to cubic had been previously reported for other very similar cathode materials such as $SrCo_{0.95}Sb_{0.05}O_{3-\delta}$[19] at temperatures of about 673 K. In the present case, the NPD diagrams collected at 300, 700, 900, and 1100 K for $Sr_{0.95}Ce_{0.05}CoO_{3-\delta}$ with λ = 1.1545 Å showed the same superstructure reflections arising from the doubling of the

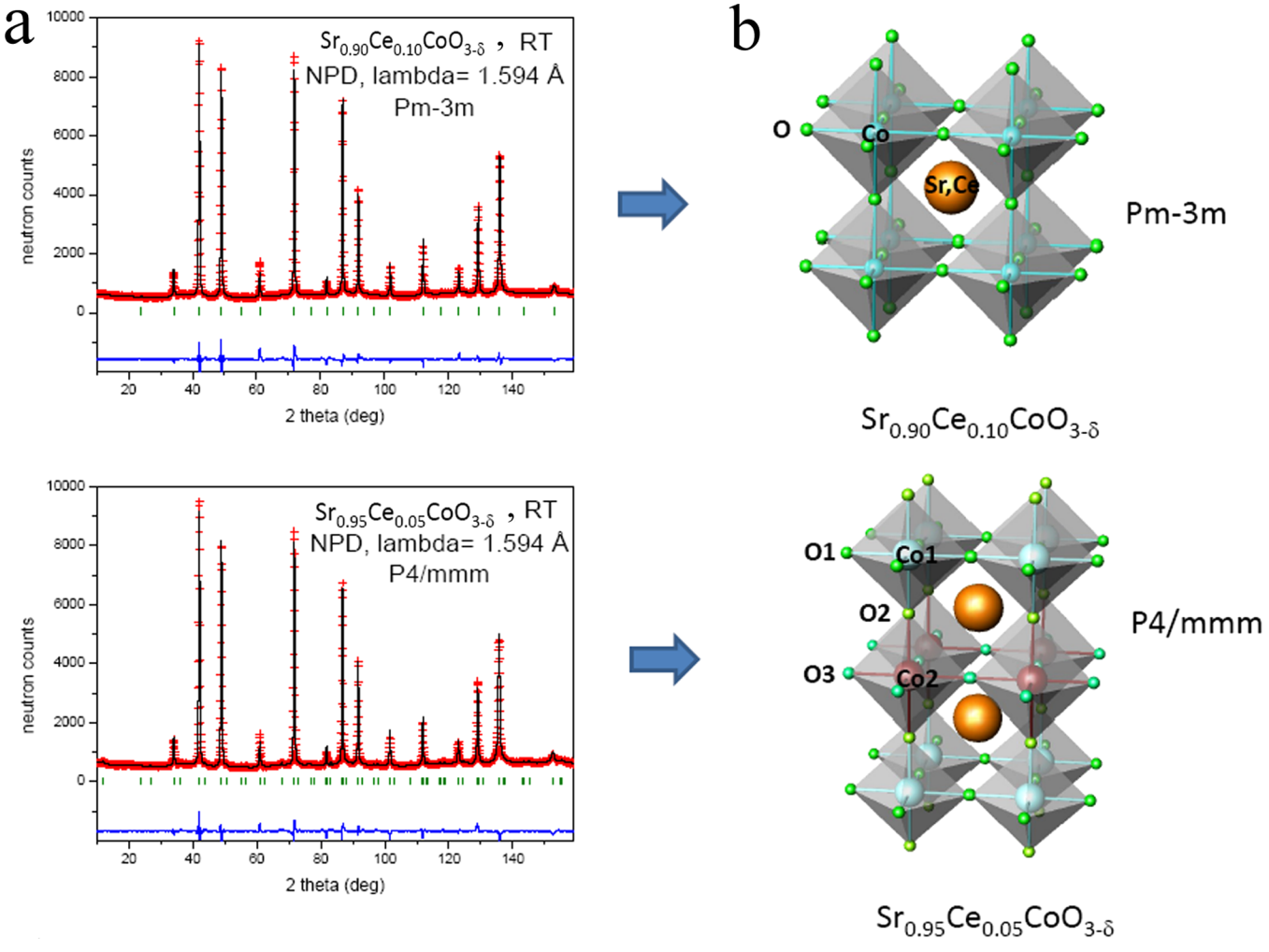

Figure 2. (a) Observed (crosses), calculated (line), and difference (bottom) NPD patterns of $Sr_{0.90}Ce_{0.10}CoO_{3-\delta}$ and $Sr_{0.95}Ce_{0.05}CoO_{3-\delta}$ at RT. (b) Corresponding crystal structures.

DOI: 10.1021/acs.inorgchem.5b00051
Inorg. Chem. 2015, 54, 3477−3484

unit cell along the *c* direction; all of the peaks could be indexed in the above-mentioned tetragonal *P*4/*mmm* unit cell, which is, therefore, demonstrated to be stable at the working conditions of the cell. Access to a wider region of the reciprocal space allowed us to successfully refine the anisotropic displacement factors for oxygen atoms, minimizing the correlation with the occupancy factor for these positions. At 300 K, a more reliable oxygen occupancy (refined from 228 reflections) of 2.67(5) is found with shorter wavelength. In fact, refinement of the oxygen occupancies reveals a severe oxygen deficiency that gradually increases with temperature, attaining the composition $Sr_{0.95}Ce_{0.05}CoO_{2.36(1)}$ at 1100 K. Figure S2 in the SI illustrates the goodness of fit in the tetragonal model for the 300 and 700 K diagrams with λ = 1.1545 Å. Table 1 contains the main structural parameters of the tetragonal structures at 300, 700, 900, and 1100 K. Table 2 lists the main interatomic distances for the different temperatures. Parts a–c of Figure 3 display thermal variation of the unit-cell parameters and volume, respectively, and parts d–f of Figure 3 show evolution of the main Co–O distances, refined from NPD data, as commented on in the Results and Discussion section. After the high-temperature experiment, a new NPD pattern was collected at 300 K (λ = 1.494 Å); the main atomic parameters after the refinement are gathered in Table S2 in the SI, and the Rietveld plot is given in Figure S3 in the SI. The main structural features are consistent with the pristine (before heating) sample; the main oxygen deficiency is concentrated at O2 and O3, as described; the global oxygen stoichiometry is 2.72(5), closer to the initial composition, which suggests that oxygen diffusion (loss and uptake) is perfectly reversible.

Table 1. Unit-Cell, Positional, and Displacement Parameters for $Sr_{0.95}Ce_{0.05}CoO_{3-\delta}$ in the Tetragonal *P*4/*mmm* (No. 123) Space Group, *Z* = 2, from NPD Data at 300, 700, 900, and 1100 K Collected with λ = 1.1545 Å

	T (K)			
	300	700	900	1100
a (Å)	3.84671(5)	3.8842(3)	3.9108(7)	3.9435(5)
c(Å)	7.7105(3)	7.7965(16)	7.869(3)	7.912(2)
V(Å^3)	114.094(4)	117.62(3)	120.35(6)	123.04(4)
Sr, Ce 2h ($^1/_2$, $^1/_2$, *z*)				
z	0.2595(4)	0.259(1)	0.262(1)	0.2644(7)
B (Å^2)	1.09(2)	1.7(1)	0.9(2)	2.77(9)
f_{occ} Sr/Ce	0.95/0.05	0.95/0.05	0.95/0.05	0.95/0.05
Co1 1a (0, 0, 0)				
B (Å^2)	0.8(1)	1.7(5)	2.6(2)	2.7(5)
Co2 1b (0, 0, $^1/_2$)				
B (Å^2)	0.7(1)	1.7(5)	2.6(2)	2.7(5)
O1 2f ($^1/_2$, 0, 0)				
B_{eq} (Å^2)[a]	2.45	2.73	5.34	8.91
f_{occ}	1.01(3)	0.98(4)	0.94(2)	0.95(3)
β_{11}	0.024(2)	0.018(3)	0.014(7)	0.096(13)
β_{22}	0.056(2)	0.018(3)	0.014(7)	0.187(30)
β_{33}	0.011(1)	0.025(4)	0.039(8)	0.036(5)
O2 2g (0, 0, *z*)				
z	0.7548(6)	0.756(2)	0.752(3)	0.752(1)
B_{eq} (Å^2)[b]	2.63	4.08	4.82	4.00
$\beta_{11} = \beta_{22}$	0.054(3)	0.076(9)	0.031(12)	0.084(13)
β_{33}	0.006(1)	0.013(3)	0.044(6)	0.006(2)
f_{occ}	0.92(5)	0.88(7)	0.92(1)	0.72(1)
O3 2e ($^1/_2$, 0, $^1/_2$)				
B_{eq} (Å^2)[b]	0.91	2.31	3.18	3.69
$\beta_{11} = \beta_{22}$	0.004(1)	0.035(8)	0.052(21)	0.043(7)
β_{33}	0.010(9)	0.011(4)	0.067(23)	0.023(4)
f_{occ}	0.75(2)	0.66(4)	0.47(1)	0.69(3)
reliability factors				
χ^2	1.95	3.45	2.31	1.46
R_{Bragg} (%)	6.14	6.33	4.62	6.12

[a]Anisotropic thermal factors $\beta_{11} \neq \beta_{22} \neq \beta_{33}$, $\beta_{12} = \beta_{13} = \beta_{23} = 0$. [b]Anisotropic thermal factors $\beta_{11} = \beta_{22} \neq \beta_{33}$, $\beta_{12} = \beta_{13} = \beta_{23} = 0$.

Table 2. Main Bond Distances (Å) for the Tetragonal $Sr_{0.05}Ce_{0.05}CoO_{3-\delta}$ Phase Determined from NPD Data at 300, 700, 900, and 1100 K (Space Group *P*4/*mmm*)

	T (K)			
	300	700	900	1100
SrO_{12} Polyhedron				
Sr–O1 (×4)	2.776(2)	2.801(7)	2.848(9)	2.875(4)
Sr–O2 (×4)	2.7223(2)	2.7490(8)	2.7701(16)	2.7916(6)
Sr–O3 (×4)	2.671(2)	2.703(7)	2.704(8)	2.713(4)
⟨Sr–O⟩	2.723	2.751	2.774	2.793
$Co1O_6$ Octahedron				
Co1–O1 (×4)	1.92339(2)	1.9421(2)	1.9554(3)	1.9720(3)
Co1–O2 (×2)	1.896(4)	1.902(16)	1.950(2)	1.957(7)
⟨Co1–O⟩	1.914	1.928	1.954	1.967
$Co2O_6$ Octahedron				
Co2–O2 (×2)	1.959(4)	1.996(16)	1.980(20)	1.998(7)
Co2–O3 (×4)	1.92339(2)	1.9421(2)	1.9554(3)	1.9720(3)
⟨Co2–O⟩	1.935	1.960	1.964	1.981

Figure 4 shows the crystal structures of the tetragonal phases, highlighting evolution of the anisotropic displacement factors at 300 and 1100 K. For O1, with occupancy factors close to unity, the thermal ellipsoids are almost spherical. However, for O2 and O3 (where most of the oxygen deficiency is concentrated), the anisotropy of the thermal ellipsoids is patent, with the largest thermal motions perpendicular to the Co–O bonds, as expected. The magnitude of the thermal motions is obviously enhanced with temperature, as shown in Table 1. At 1100 K, the occupancy factor of O3 (linking the axial positions of $Co2O_6$ octahedra) is as low as 0.66(3); Figure 4 graphically shows the orientation of the O3 ellipsoids along the [001] direction and the O2 ellipsoids on the [110] plane, suggesting a dynamical tilting of the $Co2O_6$ octahedra, which may also be interpreted as migration of the oxygen vacancies along the *c* axis, shortening and stretching the O–O distances along this direction. It is obvious that this different oxygen arrangement in successive CoO_4 layers is the driving force for the observed tetragonal superstructure, linked to oxygen positions and visible by NPD.

To further clarify the vacancy order/disorder in $Sr_{0.95}Ce_{0.05}CoO_{3-\delta}$, atomic resolution images were obtained by STEM. Figure 5A shows the unit cell of tetragonal $Sr_{0.95}Ce_{0.05}CoO_{3-\delta}$ projected along the [110] zone axis, generated by *VESTA* software[20] with the crystallographic data from the above NPD experiment. Figure 5B shows a high-angle annular dark field (HAADF) STEM image taken along the [110] zone axis. Both the A- and B-site cations can be clearly distinguished. The high-contrast rows, as shown by the white arrows, suggest ordered oxygen deficiency in the O3 site. The corresponding annular bright field (ABF) STEM image shown in Figure 5C reveals the oxygen ions in the O1 and O3 sites. The more visible oxygen ions in the O1 site than in the O3 site

DOI: 10.1021/acs.inorgchem.5b00051
Inorg. Chem. 2015, 54, 3477–3484

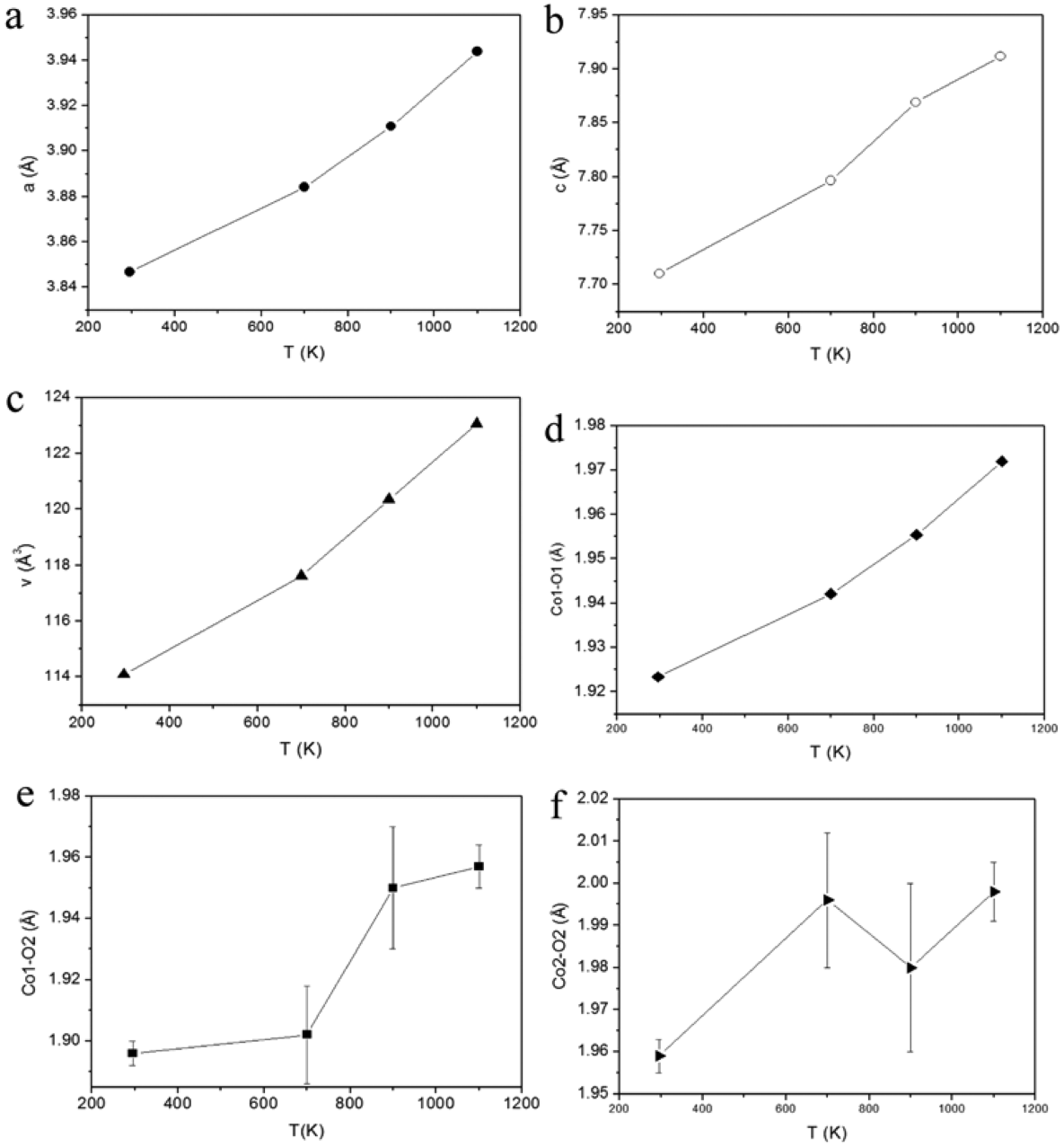

Figure 3. Thermal variation of the unit-cell parameters and volume (a–c) and evolution of the main Co–O distances (d–f). It should be noted that the error bars in parts a–d are smaller than the size of the symbols.

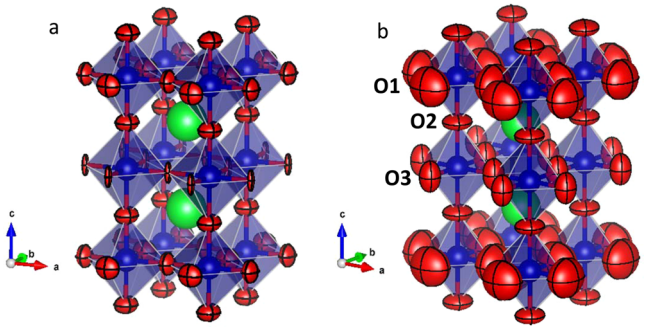

Figure 4. Crystal structures of $Sr_{0.95}Ce_{0.05}CoO_{3-\delta}$ showing the orientation of the O3 ellipsoids along the [001] direction and the O2 ellipsoids on the [110] plane at (a) RT and (b) 1100 K.

evidence the high deficiency in the O3 site, consistent with the above NPD conclusion. The ordered oxygen vacancies in $Sr_{0.95}Ce_{0.05}CoO_{3-\delta}$ are beneficial for oxygen-ion transport, thus improving the cathode performance.

3.3. Chemical Compatibility and Electrochemical Performance. The chemical compatibility between the $Sr_{0.95}Ce_{0.05}CoO_{3-\delta}$ cathode and the LSGM electrolyte was studied by grinding both materials in equal weight amounts and calcining at 1373 K for 5 h in an air atmosphere. Figure 6 shows the XRD pattern of the calcined mixture, which does not show any chemical reaction between the oxide and electrolyte, avoiding the formation of unwanted secondary phases when the material is tested in single cells.

An effective measure of the catalytic activity of the fuel cell cathode for oxygen-reduction reactions is the area-specific polarization resistance (R_p), which can be obtained from EIS

DOI: 10.1021/acs.inorgchem.5b00051
Inorg. Chem. 2015, 54, 3477–3484

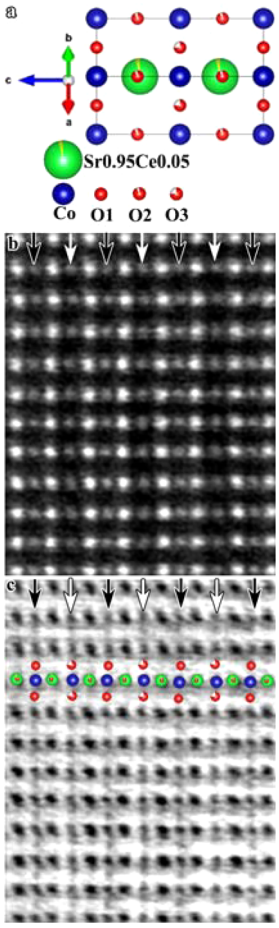

Figure 5. (A) Illustration of the unit cell of $Sr_{0.95}Ce_{0.05}CoO_{3-\delta}$ with *P4/mmm* space group projected along the [110] direction. (B) HAADF-STEM image taken along the [110] zone axis showing A/B cation sites and high contrast in the O3 site. (C) Corresponding ABF-STEM image evidencing the oxygen deficiency in the O3 site. Black and white arrows illustrate the rows of Co1O1 and Co2O3 atomic chains, respectively. Color spheres were added in the ABF image as a guide to the eyes for the positions of the atomic species (the distortion of the images is due to scanning drifting).

measurements on symmetric cathode fuel cells.[11] The EIS spectra of the symmetric cathode fuel cell measured at 1073 K are shown in Figure 7 for $Sr_{1-x}Ce_xCoO_{3-\delta}$ (x = 0.05, 0.10) after

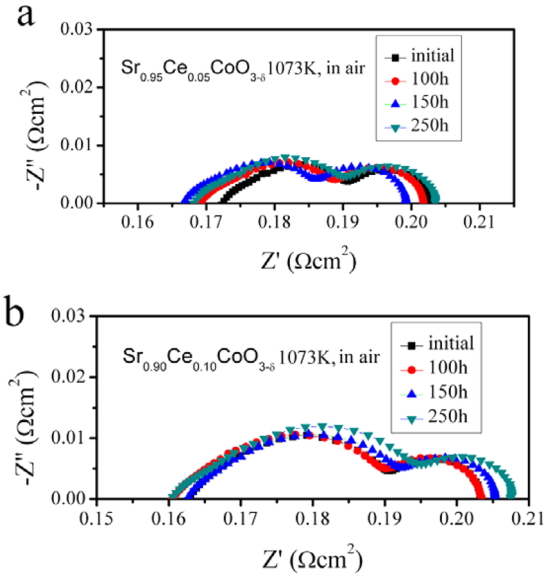

Figure 7. Comparison of impedance spectra of the $Sr_{1-x}Ce_xCoO_{3-\delta}$ cathodes tested at 1073 K and different time intervals.

several selected time intervals. It is evident that the relative values of the ohmic resistance (R_O) and R_p varied little with time for both cathode symmetric cells. The $Sr_{0.95}Ce_{0.05}CoO_{3-\delta}$ cathode cell shows a little R_p change over the entire 250 h of testing. This comparison explicitly demonstrates that the $Sr_{0.95}Ce_{0.05}CoO_{3-\delta}$ cathode possesses a superior ORR catalytic activity and stability.

The electrochemical performance of $Sr_{0.95}Ce_{0.05}CoO_{3-\delta}$ as a cathode material was reevaluated in cells Ni-SDC|LDC|LSGM|SCCO. Figure 8 shows the cell voltages and power densities as a function of the current density tested in 3 wt % H_2O humidified H_2 as the fuel and ambient air as the oxidant at the intermediate temperature range of 973−1073 K. At 973 and 1073 K, the peak power densities of the cell with $Sr_{0.95}Ce_{0.05}CoO_{3-\delta}$ reach 0.25 and 0.48 W cm^{-2}, respectively.

Our present RT NPD data clearly show that $Sr_{0.90}Ce_{0.10}CoO_{3-\delta}$ is cubic and the structure can be defined in the aristotype space group $Pm\bar{3}m$. No superstructure reflections (Figure 2a) justify the departure of this symmetry to describe the crystal structure. This is in contrast to that found by James et al.,[13] who reported a much larger unit cell $2a_0 \times 2a_0 \times 4a_0$ (space group *I4/mmm*) for this cerium-doping

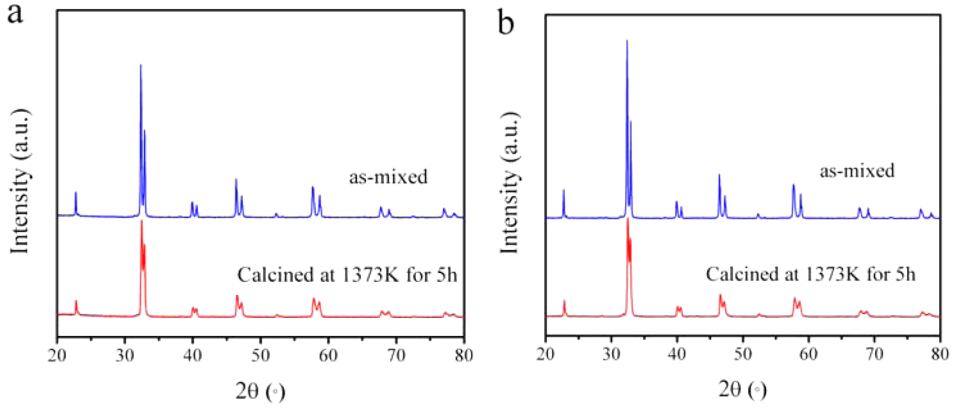

Figure 6. XRD patterns of the composites of $Sr_{0.95}Ce_{0.05}CoO_{3-\delta}$ and $Sr_{0.90}Ce_{0.10}CoO_{3-\delta}$ with LSGM calcined at 1373 K for 5 h and the as-mixed samples to show their chemical compatibility: (a) composite of $Sr_{0.95}Ce_{0.05}CoO_{3-\delta}$ and LSGM; (b) composite of $Sr_{0.90}Ce_{0.10}CoO_{3-\delta}$ and LSGM.

DOI: 10.1021/acs.inorgchem.5b00051
Inorg. Chem. 2015, 54, 3477−3484

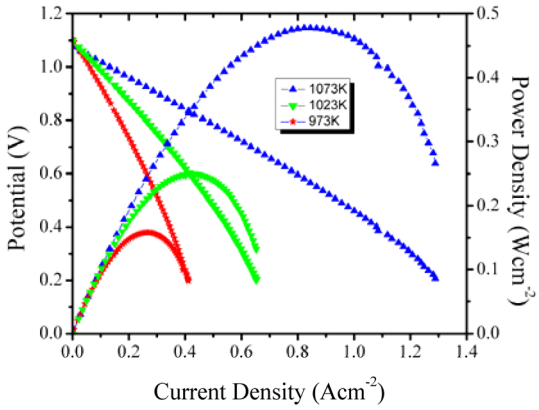

Figure 8. Cell voltage (left) and power density (right) as a function of the current density for the LSGM-electrolyte-supported cell with the $Sr_{0.95}Ce_{0.05}CoO_{3-\delta}$ cathode measured in 97% H_2/3% H_2O fuels and ambient air oxidants at 973, 1023, and 1073 K.

level. This discrepancy may be related with the different preparation procedure, by annealing in an oxygen flux for 3 days, whereas our sample was treated in air, with correspondingly lower oxygen contents, δ = 0.20 in the oxygen-annealed sample[13] and δ = 0.25 in the present case, as microscopically determined from the refinement of the oxygen occupancy factors at 300 K. It must be remarked that, for a material designed as the cathode with working temperatures up to 1123 K in an air atmosphere, an annealing in oxygen is not required.

The crystal structure of $Sr_{0.95}Ce_{0.05}CoO_{3-\delta}$ in the temperature range of 300−1100 K can be defined in a tetragonal perovskite superstructure with a doubled axis along the *c* direction, as shown in Figure 4. The oxygen vacancies are ordered; while O1 is closer to a full stoichiometry, the O2 and O3 atoms are significantly oxygen-deficient; both atoms belong to the coordination polyhedron of Co2. On the other hand, as shown in Table 2, $Co2O_6$ octahedra are elongated, with four Co2−O3 bond lengths of 1.92339(2) Å in the basal plane and two axial Co2−O2 bond lengths of 1.959(4) Å at 300 K; this conformation does not appreciably evolve in the temperature range 300−1100 K, disregarding the trend to become more regular as the temperature increases up to 1100 K. Conversely, the Co1 octahedra appear to be flattened along the *c* axial direction, exhibiting short Co1−O2 distances of 1.896(4) Å at 300 K. Thermal evolution of the four equivalent equatorial distances, also 1.92339(2) Å for this tetragonal lattice at this temperature, expands regularly as expected (Figure 4d). This long-range arrangement concerning the O2 position accounts for the observed superstructure along the *c* axis. It is remarkable that the *c*/*a* ratio slightly changes upon heating; however, one must take into consideration that, upon reduction by oxygen loss, two opposite effects come into play: the creation of vacancies should, in principle, lead to a contraction of the unit-cell dimensions, but as a consequence the associated reduction of the oxidation state of cobalt leads to an expansion of the Co−O bond lengths, thus compensating for the former effect. Therefore, besides the expected thermal expansion of *a* and *c*, there is little consequence on *c*/*a*, but a dramatic effect on the individual Co−O axial distances, as observed in Table 2 as well as Figure 3d,f, corresponding to the axial O2 atoms.

The tetragonal phase exhibits an oxygen stoichiometry spanning from 2.67(5) at 300 K to 2.36(7) at 1100 K; the average cobalt oxidation state varies accordingly between 3.24+ and 2.64+, assuming a tetravalent oxidation state for cerium. There is an alternation of small ($Co1O_6$) and large ($Co2O_6$) octahedra, with average ⟨Co−O⟩ distances of 1.914 and 1.935 Å at 300 K and 1.967 and 1.981 Å at 1100 K, respectively. The ...short−long−short... arrangement of the Co−O bond lengths suggests the establishment of a charge disproportionation or charge ordering effect across both types of cobalt cations. Given that cobalt shows an average valence of 3.24+ at 300 K, the assumption of a full charge disproportionation means an average oxidation state of $Co^{3.48+}$ at Co1 sites and Co^{3+} at Co2 positions. Therefore, the occurrence of intermediate-spin Co^{3+} at Co2 sites would account for the Jahn−Teller elongation of the Co−O bond lengths, as observed, inducing a shift of O^{2-} toward the Co^{4+} cations, thus from Co2 to Co1. At the highest temperature of 1100 K, a charge distribution $(Co1)^{3+}$−$(Co2)^{2.28+}$ is expected for a full charge disproportionation; at higher temperatures, Co^{3+} is expected to exhibit a non-Jahn−Teller high-spin state, and the plausible Co^{3+} spin transition at intermediate temperatures accounts for the nonmonotonic rearrangement of the axial distances shown in Figure 3f.

The observed performance as a MIEC oxide of $Sr_{0.95}Ce_{0.05}CoO_{3-\delta}$ is linked to the successful stabilization of a 3C-type superstructure of perovskite just by substituting 5 mol % cerium for strontium in the parent $SrCoO_{3-\delta}$ aristotype. An oxide with the starting $SrCoO_{3-\delta}$ composition invariably leads to a hexagonal 2H-like polytype containing face-sharing octahedra, with rather poor ionic and electronic transport properties below 900 °C.[6] ABO_3 perovskites consist of a close packing of AO_3 layers with B atoms placed at the all-oxygen octahedral voids; if the stacking of AO_3 layers is cubic or hexagonal, the structure is referred as 3C or 2H, which corresponds to the corner- or face-sharing arrangement of BO_6 octahedra, respectively. In fact, when the tolerance factor $[t \equiv A{-}O/\sqrt{2}(B{-}O)]$ equals unity, the ideal perovskite structure (aristotype) is stabilized, whereas the hexagonal perovskite polytypes are usually formed under ambient pressure in the ABO_3 compounds having a tolerance factor $t > 1$. In the present case, the electron-doping effect induced by the introduction of Ce^{4+} distributed at random over the Sr^{2+} dodecahedral positions drives a reduction of the tolerance factor of the perovskite (inducing the lengthening of Co−O distances), thus unstabilizing the formation of hexagonal polymorphs and yielding a corner-sharing octahedral network that favors the electronic transport.

One would be tempted to ascribe the better performance of $Sr_{1-x}Ce_xCoO_{3-\delta}$ for x = 0.05 with respect to x = 0.1 to functional factors such as the electronic conductivity; however, a prior study of this parameter for the whole series demonstrated that $Sr_{0.90}Ce_{0.1}CoO_{3-\delta}$ exhibits, by far, a better conductivity in the 673−1073 K temperature range (e.g., 400 S cm^{-1} for x = 0.1 vs 250 S cm^{-1} for x = 0.05 at 1073 K).[11] Therefore, this is not the key factor for the observed performance as a cathode material. Our present EIS data show a lower R_p for x = 0.05, indicating that it is indeed a better catalyst for the oxygen-reduction reaction. The particular oxygen vacancy arrangement exhibited by the tetragonal superstructure seems to be the reason for this catalytic performance, perhaps because it favors the interaction with adsorbed O_2 molecules prior to the reduction process. In the cubic x = 0.1 phase, the oxygen vacancies are distributed at random, whereas in the tetragonal superstructure, they are ordered over two main positions (O2 and O3), in such a way that the probabilities for an absorbed O_2 molecule to find two adjacent oxygen vacancies are much higher in the tetragonal

DOI: 10.1021/acs.inorgchem.5b00051
Inorg. Chem. 2015, 54, 3477−3484

structure. Whereas the Co1 basal plane is always fully occupied with O1 atoms, the concentration of these defects around the Co2 environment is at least $^3/_2$ times higher. Moreover, the low valence observed for Co2 (e.g., 2.28+ at 1100 K) suggests an "unsatisfied" bonding power that makes the incorporation of O_2 molecules at the adjacent oxygen vacancies easier, thus accounting for the improved performance of this material as an oxygen-reduction catalyst in SOFC.

It is also worth mentioning that very similar systems such as $SrCo_{1-x}M_xO_{3-\delta}$ (M = Sb, Mo)[9,10,19] exhibit at moderate temperatures (≈600−700 K) a phase transition from the tetragonal superstructure to the cubic aristotype, and they indeed are significantly less performing as oxygen-reduction catalysts. We conclude that the development of a tetragonal superstructure, with an ordered arrangement of oxygen vacancies, stable at the working temperature of the SOFC, seems to be the reason for the superior performance of tetragonal $Sr_{0.95}Ce_{0.05}CoO_{3-\delta}$ over related cubic phases, with the particular distribution of the oxygen vacancies enhancing the catalytic process of oxygen reduction in an intermediate-temperature SOFC.

4. CONCLUSIONS

Cerium-doped derivatives of the $SrCoO_{3-\delta}$ perovskite have been synthesized and tested as oxygen-reduction catalysts for intermediate-temperature SOFCs, competitive in power performance in the 973−1123 K temperature range. Whereas $Sr_{0.90}Ce_{0.10}CoO_{3-\delta}$ is cubic, with the oxygen vacancies distributed at random over the anion sublattice, the crystal structure of $Sr_{0.95}Ce_{0.05}CoO_{3-\delta}$ is a tetragonal superstructure with an ordered arrangement of vacancies, with the oxygen atoms showing highly anisotropic thermal motions, suggesting a dynamical tilting of the octahedra as the oxygen vacancies are diffused across the $Co2-O_4$ basal plane of the superstructure. This tetragonal network seems to be more effective in the oxygen-reduction process than the cubic aristotype. Stabilization of a 3C perovskite structure with corner-sharing CoO_6 octahedra by the introduction of only 5 mol % cerium atoms relies on the double electron injection lowering the average cobalt valence and thus reducing the tolerance factor of the perovskite, unstabilizing the face-sharing octahedra of the hexagonal 2H polytypes, which are characterized by a low electronic conductivity and present unwanted reconstructive phase transitions in the useful temperature regime of SOFCs.

■ ASSOCIATED CONTENT

Supporting Information

Unit-cell, positional, and displacement parameters, NPD patterns of $Sr_{0.95}Ce_{0.05}CoO_{3-\delta}$ collected at 300 and 700 K and again at RT after the "in-situ" high-temperature study, and impedance spectra of $Sr_{0.95}Ce_{0.05}CoO_{3-\delta}$ and $Sr_{0.90}Ce_{0.10}CoO_{3-\delta}$ symmetric cells tested at different temperature. This material is available free of charge via the Internet at http://pubs.acs.org.

■ AUTHOR INFORMATION

Corresponding Authors

*E-mail: csun@iphy.ac.cn. Tel: +86-10-82649901. Fax: +86-10-82649046.

*E-mail: ja.alonso@icmm.csic.es. Tel: +34-91-3349071. Fax: +34-91-3720623.

Notes

The authors declare no competing financial interest.

■ ACKNOWLEDGMENTS

We are grateful to the Spanish Ministry of Economy and Competitivity for granting Project MAT2013-41099-R and ILL and PSI for making all facilities available for the neutron diffraction experiments. C.S. gratefully acknowledges financial support by the National Science Foundation of China (Grants 51172275 and 51372271) and the National Key Basic Research Program of China (Grant 2012CB215402).

■ REFERENCES

(1) Sun, C. W.; Hui, R.; Roller, J. *J. Solid State Electrochem.* **2010**, *14*, 1125−1144.
(2) Deng, Z. Q.; Yang, W. S.; Liu, W.; Chen, C. S. *J. Solid State Chem.* **2006**, *179*, 362−369.
(3) Takeda, Y.; Kanno, R.; Takada, T.; Yamamoto, O.; Takano, M.; Bando, Y. *Z. Anorg. Allg. Chem.* **1986**, *541*, 259−270.
(4) De la Calle, C.; Aguadero, A.; Alonso, J. A.; Fernández-Díaz, M. T. *Solid State Sci.* **2008**, *10*, 1924−1935.
(5) Nagai, T.; Ito, W.; Sakon, T. *Solid State Ionics* **2007**, *177*, 3433−3444.
(6) Deng, Z. Q.; Liu, W.; Chen, C. S.; Lu, H.; Yang, W. S. *Solid State Ionics* **2004**, *170*, 187−190.
(7) Zeng, P.; Ran, R.; Chen, Z.; Zhou, W.; Gu, H.; Shao, Z.; Liu, S. *J. Alloys Compd.* **2008**, *455*, 465−470.
(8) Chen, X.; Huang, L.; Wei, Y.; Wang, H. *J. Membr. Sci.* **2011**, *368*, 159−164.
(9) Aguadero, A.; De la Calle, C.; Alonso, J. A.; Escudero, M. J.; Fernandez-Díaz, M. T.; Daza, L. *Chem. Mater.* **2007**, *19*, 6437−6344.
(10) Aguadero, A.; Perez-Coll, D.; Alonso, J. A.; Skinner, S. J.; Kilner, J. *Chem. Mater.* **2012**, *24*, 2655−2663.
(11) Yang, W.; Hong, T.; Sun, C. W.; Xia, C. R.; Chen, L. Q. *ACS Appl. Mater. Interfaces* **2013**, *5*, 1143−1148.
(12) Trofimenko, N. E.; Paulsen, J.; Ullmann, H.; Müller, R. *Solid State Ionics* **1997**, *100*, 183−191.
(13) James, M.; Wallwork, K. S.; Withers, R. L.; Goossens, D. J.; Wilson, K. F.; Horvat, J.; Wang, X. L.; Colella, M. *Mater. Res. Bull.* **2005**, *40*, 1415−1431.
(14) Maignan, A.; Raveau, B.; Ḥebert, S.; Pralong, V.; Caignaert, V.; Pelloquin, D. *J. Phys.: Condens. Matter.* **2006**, *18*, 4305−4314.
(15) Wei, Q. T.; Guo, R. S.; Wang, F. H.; Li, H. *J. Mater. Sci.* **2005**, *40*, 1317−1319.
(16) Yang, W.; Salim, J.; Li, S.; Sun, C. W.; Chen, L. Q.; Goodenough, J. B.; Kim, Y. *J. Mater. Chem.* **2012**, *22*, 18902−18907.
(17) Kim, J. K.; Yang, W.; Salim, J.; Ma, C.; Sun, C. W.; Li, J. Q.; Kim, Y. *J. Electrochem. Soc.* **2014**, *161*, A285−A289.
(18) Rodríguez-Carvajal, J. *Physica B* **1993**, *192*, 55−69.
(19) Aguadero, A.; Alonso, J. A.; Pérez-Coll, D.; de la Calle, C.; Fernández-Díaz, M. T.; Goodenough, J. B. *Chem. Mater.* **2010**, *22*, 789−798.
(20) Momma, K.; Izumi, F. *J. Appl. Crystallogr.* **2011**, *44*, 1272−1276.

DOI: 10.1021/acs.inorgchem.5b00051
Inorg. Chem. 2015, 54, 3477−3484